Multilayer-HySEA model validation for landslide generated tsunamis. Part II Granular slides

Jorge Macías*, Cipriano Escalante, Manuel J. Castro

Departamento de Análisis Matemático, Estadística e Investigación Operativa y Matemática Aplicada, Facultad de Ciencias, Universidad de Málaga, 29080-Málaga

Abstract

The final aim of the present work is to propose a NTHMP-benchmarked numerical tool for landslide generated tsunami hazard assessment. To achieve this, the novel Multilayer-HySEA model is validated using laboratory experiment data for landslide generated tsunamis. In particular, this second part of the work deals with granular slides, while the first part, in a companion paper, considers rigid slides. The experimental data used have been proposed by the US National Tsunami Hazard and Mitigation Program (NTHMP) and were established for the NTHMP Landslide Benchmark Workshop, held in January 2017 at Galveston (Texas). Three of the seven benchmark problems proposed in that workshop dealt with tsunamis generated by rigid slides and are collected in the companion paper (Macías et al., 2020a). Another three benchmarks considered tsunamis generated by granular slides. They are the subject of the present study. The seventh benchmark problem proposed the field case of Port Valdez Alaska 1964 and can be found in Macías et al. (2017). In order to reproduce the laboratory experiments dealing with granular slides, two models need to be coupled, one for the granular slide and a second one for the water dynamics. The coupled model used consists of a new and efficient hybrid finite-volume/finite-difference implementation on GPU architectures of a non-hydrostatic multilayer model coupled with a Savage-Hutter model. To introduce the multilayer model more fluidly, we first present the equations of the one-layer model, Landslide-HySEA, with both strong and weak couplings between the fluid layer and the granular slide. Then, a brief description of the multilayer model equations and the numer-

---

*Corresponding author

Email address: jmacias@uma.es (Jorge Macías)

January 16, 2021

ical scheme used is included. The dispersive properties of the multilayer model can be found in the companion paper. Then, results for the three NTHMP benchmark problems dealing with tsunamis generated by granular slides are presented with a description of each benchmark problem.

Keywords: Multilayer-HySEA model, tsunamis, granular slides, model benchmarking, landslide-generated tsunamis, NTHMP, GPU implementation
2010 MSC: 35L, 65-05, 76-05, 86-08

1. Introduction

Following the introduction of the companion paper Macías et al. (2020a), a landslide tsunami model benchmarking and validation workshop was held, January 9-11, 2017, in Galveston, TX. This workshop, which was organized on behalf of NOAA-NWS's National Tsunami Hazard Mitigation Program (NTHMP) Mapping and Modeling Subcommittee (MMS), with the expected outcome being to develop: (i) a set of community accepted benchmark tests for validating models used for landslide tsunami generation and propagation in NTHMP inundation mapping work; (ii) workshop documentation and a web-based repository, for benchmark data, model results, and workshop documentation, results, and conclusions, and (iii) provide recommendations as a basis for developing best practice guidelines for landslide tsunami modeling in NTHMP work.

A set of seven benchmark tests was selected (Kirby et al., 2018). The selected benchmarks were taken from a subset of available laboratory data sets for solid slide experiments (three of them) and deformable slide experiments (another three), that included both submarine and subaerial slides. Finally, a benchmark based on a historic field event (Valdez, AK, 1964) closed the list of proposed benchmarks. The EDANYA group (www.uma.es/edanya) from the University of Malaga participated in the aforementioned workshop, and the numerical codes Multilayer-HySEA and Landslide-HySEA were used to produce our modeled results. We presented numerical results for six out of the seven benchmark problems proposed, including the field case (Macías et al., 2017). The sole benchmark we did not perform at the time was BP6, for which numerical results

are included here.

The present work aims at showing the numerical results obtained with the Multilayer-HySEA model in the framework of the validation effort described above for the case of granular slide generated tsunamis for the complete set of the three benchmark problems proposed by the NTHMP. However, the ultimate goal of the present work is to provide the tsunami community with a numerical tool, tested and validated meeting the defined criteria for the NTHMP, for landslide generated tsunami hazard assessment. This NTHMP-acceptance has already been achieved by the Tsunami-HySEA model for the case of earthquake generated tsunamis (Macías et al., 2017; Macías et al., 2020c,d).

Fifteen years ago, at the beginning of the century, solid block landslide modeling challenged researchers and was undertaken by a number of authors (see companion paper Macías et al. (2020a) for references) and laboratory experiments were developed for those cases and for tsunami model benchmarking. In contrast, some early models (e.g., Heinrich (1992); Harbitz et al. (1993); Rzadkiewicz et al. (1997); Fine et al. (1998)) and a number of more recent models have simulated tsunami generation by deformable slides, based either on depth-integrated two-layer model equations, or on solving more complete sets of equations in terms of featured physics (dispersive, non-hydrostatic, Navier-Stokes). Examples include solutions of 2D or 3D Navier-Stokes equations to simulate subaerial or submarine slides modeled as dense Newtonian or non-Newtonian fluids (Ataie-Ashtiani and Shobeyri, 2008; Weiss et al., 2009; Abadie et al., 2010, 2012; Horrillo et al., 2013), flows induced by sediment concentration (Ma et al., 2013), or fluid or granular flow layers penetrating or failing underneath a 3D water domain (for example, the two-layer models of Macías et al. (2015) or González-Vida et al. (2019) where a fully coupled non-hydrostatic SW/Savage-Hutter model is used or the model used in Ma et al. (2015); Kirby et al. (2016) in which the upper water layer is modeled with the non-hydrostatic σ-coordinate 3D model NHWAVE (Ma et al., 2012). For a more comprehensive review of recent modeling work, see Yavari-Ramshe and Ataie-Ashtiani (2016). A number of recent laboratory experiments have modeled tsunamis generated by

subaerial landslides composed of gravel (Fritz et al. (2004), Ataie-Ashtiani and Najafi-Jilani (2008), Heller and Hager (2010), Mohammed and Fritz (2012)) or glass beads (Viroulet et al., 2014). For deforming underwater landslides and related tsunami generation, 2D experiments were performed by Rzadkiewicz et al. (1997), who used sand, and Ataie-Ashtiani and Najafi-Jilani (2008), who used granular material. Well-controlled 2D glass bead experiments were reported and modeled by Grilli et al. (2017) using the model of Kirby et al. (2016).

The benchmark problems performed in the present work are based on the laboratory experiments of Kimmoun and Dupont (see Grilli et al. (2017)) for BP4, Viroulet et al. (2014) for BP5, and Mohammed and Fritz (2012) for BP6. The basic reference for these three benchmarks, but also the three ones related to solid slides and the Alaska field case, all of them proposed by the NTHMP, is Kirby et al. (2018). That is a key reference for readers interested in the benchmarking initiative which the present work is based on.

2. The Landslide-HySEA model for granular slides

First we consider the Landslide-HySEA model, applied in Macías et al. (2015) and González-Vida et al. (2019), which for the case of one-dimensional domains reads:

$$
\begin{cases}
\partial_t h + \partial_x \left(hu \right) = 0, \\
\partial_t \left(hu \right) + \partial_x \left(hu^2 + \dfrac{1}{2} g h^2 \right) - g h \partial_x \left(H - z_s \right) = n_a (u_s - u), \\
\partial_t z_s + \partial_x \left(z_s u_s \right) = 0, \\
\partial_t \left(z_s u_s \right) + \partial_x \left(z_s u_s^2 + \dfrac{1}{2} g \left(1 - r \right) z_s^2 \right) = g z_s \partial_x \left(\left(1 - r \right) H - r\eta \right) \\
\hspace{5cm} - r n_a (u_s - u) + \tau_P,
\end{cases}
\tag{1}
$$

where g is the gravity acceleration ($g = 9.81 \ m/s^2$); $H(x)$ is the non-erodible (do not evolve in time) bathymetry measured from a given reference level; $z_s(x,t)$ represents the thickness of the layer of granular material at each point x at time t; $h(x,t)$ is the total water depth; $\eta(x,t)$ denotes the free surface (measured form the same fixed reference level used for the bathymetry, for example, the mean

sea surface) and is given by $\eta = h + z_s - H$; $u(x,t)$ and $u_s(x,t)$ are the averaged horizontal velocity for the water and for the granular material, respectively; $r = \frac{\rho_1}{\rho_2}$ is the ratio of densities between the ambient fluid and the granular material. The term $n_a(u_s - u)$ parameterizes the friction between the fluid and the granular layer. Finally, the term $\tau_P(x,t)$ represents the friction between the granular slide and the non-erodible bottom surface. It is parameterized as in Pouliquen and Forterre (2002) and it will be described in the next section.

System (1) presents the difficulty of considering the complete coupling between sediment and water, including the corresponding coupled pressure terms. That makes its numerical approximation more complex. Moreover, it makes also difficult to consider its natural extension to non-hydrostatic flows.

Now, if $\partial_x \eta$ is neglected in the momentum equation of the granular material, that is, the fluctuation of pressure due to the variations of the free-surface are neglected in the momentum equation of the granular material, then the following weakly-coupled system could be obtained:

$$
\text{S-W system} \quad
\begin{cases}
\partial_t h + \partial_x (hu) = 0, \\
\partial_t (hu) + \partial_x \left(hu^2 + \dfrac{1}{2}gh^2 \right) - gh\partial_x (H - z_s) = n_a(u_s - u),
\end{cases}
\tag{2}
$$

$$
\text{S-H system} \quad
\begin{cases}
\partial_t z_s + \partial_x (z_s u_s) = 0, \\
\partial_t (z_s u_s) + \partial_x \left(z_s u_s^2 + \dfrac{1}{2}g(1-r) z_s^2 \right) - g(1-r) z_s \partial_x H = \\
\qquad\qquad\qquad\qquad\qquad\qquad\qquad\qquad -rn_a(u_s - u) + \tau_P,
\end{cases}
\tag{3}
$$

where the first system is the standard one-layer shallow-water system and the second one is the one-layer reduced-gravity Savage-Hutter model (Savage and Hutter (1989)), that takes into account that the granular landslide is underwater. Note that the previous system could be also adapted to simulate subaerial/submarine landslides by a suitable treatment of the variation of the gravity terms. Under this formulation, it is now straightforward to improve the

numerical model for the fluid phase by including non-hydrostatic effects.

In the present study, the governing equations of the landslide motion are derived in Cartesian coordinates. In some cases where steep slopes are involved, landslide models based on local coordinates allow representing the slide motion better. However, when general topographies are considered and not only simple geometries, landslide models based on local coordinates also introduce some difficulties on the final numerical model and on its implementation compromising, at the same time, the computational efficiency of the numerical model. Here, we focus on the hydrodynamic component of the system, and that is one of the reasons for choosing a simple landslide model based on Cartesian coordinates. Of course, the strategies presented here can also be adapted for more sophisticated landslide models. For example, in Garres-Daz et al. (2020) a non-hydrostatic model for the hydrodynamic part that is similar to the one presented here for the case of a single layer was introduced. In the work mentioned above, the authors study the influence of coupling the hydrodynamic model with a granular model that is derived in both reference systems: Cartesian and local coordinates. The front positions calculated with the Cartesian model progress faster and, after some time, they are slightly ahead compared with the local coordinate model solution (see, for instance, Figure 4 in Garres-Daz et al. (2020)). This is due to the fact that the Cartesian model uses the horizontal velocity instead of the velocity tangent to the topography. In any case, the differences between the two models are not very noticeable. A granular slide model based on local coordinates might gives better results. However, when introducing a non-hydrostatic pressure, the model is closer to a 3D solver. In such a case, the influence on the reference coordinate system barely exists. That is the reason why in Garres-Daz et al. (2020), both non-hydrostatic models based on different coordinate systems show similar results. In any case, although on the present work we focus on the hydrodynamic part, it can be observed on the benchmark tests that the numerical results are in very good agreement with the laboratory measured data, despite the simple landslide model chosen here.

3. The Multilayer-HySEA model

The Multilayer-HySEA model implements a two-phase model intended to reproduce the interaction between the slide granular material (submarine or subaerial) and the fluid. In the present work, a multi-layer non-hydrostatic shallow-water model is considered for modeling the evolution of the ambient water (see Fernández-Nieto et al. (2018)), and for simulating the kinematics of the submarine/subaerial landslide the Savage-Hutter model (3) is used. The coupling between these two models is performed through the boundary conditions at their interface. The parameter r represents the ratio of densities between the ambient fluid and the granular material (slide liquefaction parameter). Usually

$$r = \frac{\rho_f}{\rho_b}, \quad \rho_b = (1 - \varphi)\rho_s + \varphi \rho_f, \tag{4}$$

where ρ_s stands for the typical density of the granular material, ρ_f is the density of the fluid ($\rho_s > \rho_f$) both constant, and φ represents the porosity ($0 \leq \varphi < 1$). In the current work, the porosity, φ, is supposed to be constant in space and time and, therefore, the ratio r is also constant. This ratio ranges from 0 to 1 (i.e. $0 < r < 1$) and, even on a uniform material is difficult to estimate as it depends on the porosity (and ρ_f and ρ_s are also supposed constant). Typical values for r are in the interval $[0.3, 0.8]$.

The fluid model

The ambient fluid is modeled by a multi-layer non-hydrostatic shallow-water system (Fernández-Nieto et al., 2018) to account for dispersive water waves. The model considered, that is obtained by a process of depth-averaging of the Euler equations, can be interpreted as a semi-discretization with respect to the vertical coordinate. In order to take into account dispersive effects, the total pressure is decomposed into the sum of hydrostatic and non-hydrostatic components. In this process, the horizontal and vertical velocities are supposed to have constant vertical profiles. The resulting multi-layer model admits an exact energy balance, and when the number of layers increases, the linear dispersion
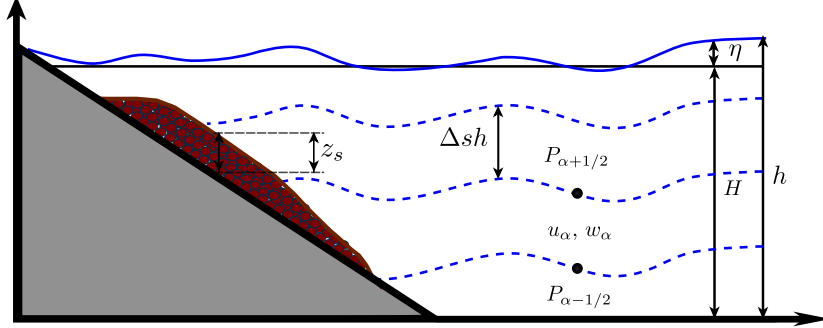
Figure 1: Schematic diagram describing the multilayer system

relation of the linear model converges to the same of Airy's theory. Finally, the model proposed in Fernández-Nieto et al. (2018) can be written in compact form as:

$$
\begin{cases}
\partial_t h + \partial_x (hu) = 0, \\
\partial_t (hu_\alpha) + \partial_x \left(hu_\alpha^2 + \frac{1}{2}gh^2 \right) - gh\partial_x (H - z_s) \\
\qquad + u_{\alpha+1/2}\Gamma_{\alpha+1/2} - u_{\alpha-1/2}\Gamma_{\alpha-1/2} = -h\left(\partial_x p_\alpha + \sigma_\alpha \partial_z p_\alpha\right) - \tau_\alpha \\
\partial_t (hw_\alpha) + \partial_x (hu_\alpha w_\alpha) + w_{\alpha+1/2}\Gamma_{\alpha+1/2} - w_{\alpha-1/2}\Gamma_{\alpha-1/2} = -h\partial_z p_\alpha, \\
\partial_x u_{\alpha-1/2} + \sigma_{\alpha-1/2}\partial_z u_{\alpha-1/2} + \partial_z w_{\alpha-1/2} = 0,
\end{cases}
\tag{5}
$$

for $\alpha \in \{1, 2, \ldots, L\}$, with L the number of layers and where the following notation has been used:

$$
f_{\alpha+1/2} = \frac{1}{2}\left(f_{\alpha+1} + f_\alpha\right), \ \partial_z f_{\alpha+1/2} = \frac{1}{h\Delta s}\left(f_{\alpha+1} - f_\alpha\right),
$$

where f denotes one of the generic variables of the system, i.e., u, w and p; $\Delta s = 1/L$ and, finally,

$$
\sigma_\alpha = \partial_x \left(H - z_s - h\Delta s(\alpha - 1/2)\right), \ \sigma_{\alpha-1/2} = \partial_x \left(H - z_s - h\Delta s(\alpha - 1)\right).
$$

Figure 1 shows a schematic picture of model configuration, where the total water height h is decomposed along the vertical axis into $L \geq 1$ layers. The depth-averaged velocities in the x and z directions are written as u_α and w_α, respectively. The non-hydrostatic pressure at the interface $z_{\alpha+1/2}$ is denoted by $p_{\alpha+1/2}$. The free surface elevation measured from a fixed reference level (for

example the still-water level) is written as η and $\eta = h - H + z_s$, where again $H(x)$ is the unchanged non-erodible bathymetry measured from the same fixed reference level. $\tau_\alpha = 0$, for $\alpha > 1$ and τ_1 is given by

$$\tau_1 = \tau_b - n_a(u_s - u_1),$$

where τ_b stands for an classical Manning-type parameterization for the bottom shear stress and, in our case, is given by

$$\tau_b = gh\frac{n^2}{h^{4/3}}u_1|u_1|,$$

and $n_a(u_s - u_1)$ accounts for the friction between the fluid and the granular layer. The latest two terms are only present at the lowest layer ($\alpha = 1$). Finally, for $\alpha = 1, \ldots, L - 1$, $\Gamma_{\alpha+1/2}$ parameterizes the mass transfer across interfaces and those terms are defined by

$$\Gamma_{\alpha+1/2} = \sum_{\beta=\alpha+1}^{L} \partial_x \left(h\Delta s \left(u_\beta - \bar{u} \right) \right), \ \bar{u} = \sum_{\alpha=1}^{L} \Delta s u_\alpha$$

Here we suppose that $\Gamma_{1/2} = \Gamma_{L+1/2} = 0$, this means that there is no mass transfer through the sea-floor or the water free-surface. In order to close the system, the boundary condition

$$p_{L+1/2} = 0,$$

is imposed at the free surface and the boundary conditions

$$u_0 = 0, \ w_0 = -\partial_t \left(H - z_s \right),$$

are imposed at the bottom. The last two conditions enter into the incompressibility relation for the lowest layer ($\alpha = 1$), given by

$$\partial_x u_{1/2} + \sigma_{1/2}\partial_z u_{1/2} + \partial_z w_{1/2} = 0.$$

It should be noted that both models, the hydrodynamic model described here and the morphodynamic model described in the next subsection, are coupled through the unknown z_s, that, in the case of the model described here, it is present in the equations and in the boundary condition ($w_0 = -\partial_t \left(H - z_s \right)$).

Some dispersive properties of the system (5) were originally studied in Fernández-Nieto et al. (2018). Moreover, for a better-detailed study on the dispersion relation (such as 'phase velocity', 'group velocity', and 'linear shoaling') the reader is referred to the companion paper Macías et al. (2020a).

Along the derivation of the hydrodynamic model presented here, the rigid-lid assumption for the free surface of the ambient fluid is adopted. This means that pressure variations induced by the fluctuation on the free surface of the ambient fluid over the landslide are neglected.

The Landslide model

The 1D Savage-Hutter model used and implemented in the present work is given by the system (3). The friction law τ_P (Pouliquen and Forterre (2002)) is given by the expression,

$$\tau_P = -g\left(1 - r\right)\mu z_s \frac{u_s^2}{|u_s|},$$

where μ is a constant friction coefficient with a key role, as it controls the movement of the landslide. Usually μ is given by the Coulomb friction law as the simpler parameterization that can be used in landslide models. However, it is well-known that a constant friction coefficient does not allow to reproduce steady uniform flows over rough beds observed in the laboratory for a range of inclination angles. To reproduce these flows, in Pouliquen and Forterre (2002), the authors introduce an empirical friction coefficient μ that depends on the norm of the mean velocity u_s, on the thickness z_s of the granular layer and on the Froude number $Fr = \frac{u_s}{\sqrt{gz_s}}$. The friction law is given by:

$$\mu(z_s, u_s) = \begin{cases} \mu_{\text{start}}(z_s) + \left(\dfrac{Fr}{\beta}\right)^{\gamma}\left(\mu_{\text{stop}}(z_s) - \mu_{\text{start}}(z_s)\right), & \text{for } Fr < \beta, \\ \mu_{\text{stop}}(z_s), & \text{for } \beta \leq Fr, \end{cases}$$

with

$$\mu_{\text{start}}(z_s) = \tan(\delta_3) + (\tan(\delta_2) - \tan(\delta_1))\, exp\left(-\frac{z_s}{d_s}\right)$$

$$\mu_{\text{stop}}(z_s) = \tan(\delta_1) + (\tan(\delta_2) - \tan(\delta_1))\, exp\left(-\frac{z_s\beta}{d_s Fr}\right)$$

where d_s represents the mean size of grains. $\beta = 0.136$ and $\gamma = 10^{-3}$ are empirical parameters. $\tan(\delta_1)$, $\tan(\delta_2)$ are the characteristic angles of the material, and $\tan(\delta_3)$ is other friction angle related to the behavior when starting from rest. This law has been widely used in the literature (see e.g. Brunet et al. (2017)).

Note that the slide model can also be adapted to simulate subaerial landslides. The presence of the term $(1 - r)$ in the definition of the Poulilquen-Folterre friction law is due to the buoyancy effects, which must be taken into account only in the case that the granular material layer is submerged in the fluid. Otherwise, this term must be replaced by 1.

4. Numerical Solution Method

System (3) can be written in the following compact form:

$$\partial_t U_s + \partial_x F_s \left(U_s \right) = G_s \left(U_s \right) \partial_x H - S_s \left(U_s \right), \tag{6}$$

being

$$U_s = \begin{bmatrix} z_s \\ u_s z_s \end{bmatrix}, \quad F_s \left(U_s \right) = \begin{bmatrix} z_s u_s \\ z_s u_s^2 + \dfrac{1}{2} g \left(1 - r \right) z_s^2 \end{bmatrix},$$

$$G_s(U_s) = \begin{bmatrix} 0 \\ g \left(1 - r \right) z_s \end{bmatrix}, \quad S_s \left(U_s \right) = \begin{bmatrix} 0 \\ -r n_a (u_s - u) + \tau_P \end{bmatrix}.$$

Analogously, the multi-layer non-hydrostatic shallow-water system (5) can also be expressed in a similar way:

$$\begin{cases} \partial_t U_f + \partial_x F_f(U_f) + B_f(U_f)\partial_x U_f = G_f(U)\partial_x(H - z_s) + \mathcal{T}_{NH} - S_f(U_f), \\ B(U_f, (U_f)_x, H, H_x, z_s, (z_s)_x) = 0, \end{cases} \tag{7}$$

where

$$
U_f = \begin{bmatrix} h \\ hu_1 \\ \vdots \\ hu_L \\ hw_1 \\ \vdots \\ hw_L \end{bmatrix}, F_f(U_f) = \begin{bmatrix} h\bar{u} \\ hu_1^2 + \dfrac{1}{2}gh^2 \\ \vdots \\ hu_L^2 + \dfrac{1}{2}gh^2 \\ hu_1 w_1 \\ \vdots \\ hu_L w_L \end{bmatrix}, G_f(U_f) = \begin{bmatrix} 0 \\ gh \\ \vdots \\ gh \\ 0 \\ \vdots \\ 0 \end{bmatrix}.
$$

and $B_f(U_f)\partial_x(U_f)$ contains the non-conservative products involving the momentum transfer across the interfaces and, finally, $S_f(U_f)$ represents the friction terms:

$$
B_f(U_f)\partial_x(U_f) = \begin{bmatrix} 0 \\ u_{3/2}\Gamma_{3/2} \\ u_{5/3}\Gamma_{5/2} - u_{3/2}\Gamma_{3/2} \\ \vdots \\ -u_{L-1/2}\Gamma_{L-1/2} \\ w_{3/2}\Gamma_{3/2} \\ w_{5/3}\Gamma_{5/2} - w_{3/2}\Gamma_{3/2} \\ \vdots \\ -w_{L-1/2}\Gamma_{L-1/2} \end{bmatrix}, \quad S_f(U_f) = \begin{bmatrix} 0 \\ \tau_b - n_a(u_s - u_1) \\ 0 \\ \vdots \\ 0 \end{bmatrix}.
$$

The non-hydrostatic corrections in the momentum equations are given by

$$
\mathcal{T}_{NH} = \mathcal{T}_{\mathcal{NH}}(h, h_x, H, H_x, z_s, (z_s)_x, p, p_x) = - \begin{bmatrix} 0 \\ h(\partial_x p_1 + \sigma_1 \partial_z p_1) \\ \vdots \\ h(\partial_x p_L + \sigma_L \partial_z p_L) \\ h\partial_z p_1 \\ \vdots \\ h\partial_z p_L \end{bmatrix},
$$

and finally, the operator related with the incompressibility condition at each layer is given by:

$$B(U_f,(U_f)_x,H,H_x,z_s,(z_s)_x) = \begin{bmatrix} \partial_x u_{1/2} + \sigma_{1/2}\partial_z u_{1/2} + \partial_z w_{1/2} \\ \vdots \\ \partial_x u_{L-1/2} + \sigma_{L-1/2}\partial_z u_{L-1/2} + \partial_z w_{L-1/2} \end{bmatrix}.$$

The discretization of systems (6) and (7) becomes difficult. In the present work, the natural extension of the numerical schemes proposed in Escalante et al. (2018a,b) is considered. These authors propose, describe and use a splitting technique. Initially, the systems (6) and (7) are expressed as the following non-conservative hyperbolic system:

$$\begin{cases} \partial_t U_s + \partial_x F_s(U_s) = G_s(U_s)\partial_x H, \\ \partial_t U_f + \partial_x F_f(U_f) + B_f(U_f)\partial_x(U_f) = G_f(U_f)\partial_x(H - z_s). \end{cases} \tag{8}$$

Both equations are solved simultaneously using a second order HLL (Harten-Lax-van Leer), positivity-preserving and well-balanced, path-conservative finite volume scheme (see Castro and Fernández-Nieto (2012)) and using the same *time step*. The synchronization of time steps is performed by taking into account the CFL condition of the complete system (8). A first order estimation of the maximum of the wave speed for system (8) is the following:

$$\lambda_{\max} = \max(|u_s| + \sqrt{(g(1-r)z_s}, |\bar{u}| + \sqrt{gh}).$$

Then, the non-hydrostatic pressure corrections $p_{1/2}, \cdots, p_{L-1/2}$ at the vertical interfaces are computed from

$$\begin{cases} \partial_t U_f = \mathcal{T}_{NH}(h, h_x, H, H_x, z_s, (z_s)_x, p, p_x), \\ B(U_f, (U_f)_x, H, H_x, z_s, (z_s)_x) = 0 \end{cases}$$

which requires the discretization of an elliptic operator that is done using standard second-order central finite differences. This results in a linear system than in our case it is solved using an iterative Scheduled Jacobi method (see Adsuara et al. (2016)). Finally, the computed non-hydrostatic correction are used to update the horizontal and vertical momentum equations at each layer and, at the

same time, the frictions $S_s(U_s)$ and $S_f(U_f)$ are also discretized (see Escalante et al. (2018a,b)). For the discretization of the Coulomb friction term, we refer the reader to Fernández-Nieto et al. (2008).

The resulting numerical scheme is well-balanced for the water at rest stationary solution and is linearly L^∞-stable under the usual CFL condition related to the hydrostatic system. It is also worth mentioning that the numerical scheme is positive preserving and can deal with emerging topographies. Finally, its extension to 2D is straightforward. For dealing with numerical experiments in 2D regions, the computational domain must be decomposed into subsets with a simple geometry, called cells or finite volumes. The 2D numerical algorithm for the hydrodynamic hyperbolic component of the coupled system is well suited to be parallelized and implemented in GPU architectures, as is shown in Castro et al. (2011). Nevertheless, a standard treatment of the elliptic part of the system do not allow the parallelization of the algorithms. The method used here and proposed in Escalante et al. (2018a,b)), makes it possible that the second step can also be implemented on GPUs, due to the compactness of the numerical stencil and the easy and massively parallelization of the Jacobi method The above-mentioned parallel GPU and multi-GPU implementation of the complete algorithm results in much shorter computational times.

5. Benchmark Problem Comparisons

This section presents the numerical results obtained with the Multilayer-HySEA model for the three benchmark problems dealing with granular slides and the comparison with the measured lab data for the generated water waves. In particular, BP4 deals with a 2D submarine granular slide, BP5 with a 2D subaerial slide, and BP6 with a 3D subaerial slide. The description of all these benchmarks can be found at LTMBW (2017) and Kirby et al. (2018). In this paper, all units, unless otherwise indicated, will be expressed in the International System of Units (IS).

The model parameters required at each simulation are:

$$g, \; r, \; n_a, \; n_m, \; d_s, \; \delta_i, \; \beta, \text{and } \gamma.$$

The parameters $g, \; r, \; n_m,$ and d_s are related to physical settings given at each experiment. β and γ are empirical parameters that were chosen as in the seminal paper of Pouliquen and Forterre (2002).

The friction angles δ_1 and δ_2 are characteristic angles of the material, and δ_3 is related to the behavior of the slide motion when starting from the rest. Thus, the values of these angles strongly depend on the granular material. They were adjusted within a range of feasible values according to the references (Brunet et al. (2017), Mangeney et al. (2007), and Pouliquen and Forterre (2002)):

$$\delta_1 \in [1°, 22°], \quad \delta_2 \in [11°, 34°], \quad \delta_3 \in [3°, 23°].$$

In the present paper we have used the values

$$\delta_1 = 6°, \quad \delta_2 \in [17°, 30°], \quad \delta_3 = 12°,$$

for the three benchmark problems, which is consistent with the values found in the literature. As noted in Mangeney et al. (2007), in general for real problems involving complex rheologies, smaller values of these parameters δ_i should be employed.

With regard to the sensitivity of the model to parameter variation, an appropriate sensitivity analysis can be performed, as it is done in González-Vida et al. (2019). However, the aim of the present work was to prove if the non-hydrostatic model couple with the granular model was able to accurately reproduce the three benchmarks considered.

Regarding the parameter denoting the buoyancy effect, for field cases, $r = 0.5$ is usually taken, and then the parameter is eventually adjusted based on available field data. In general, the complexity of the rheology introduces a difficulty that is always present on the modelling as well as on the adjustment of the parameters. Moreover, the more sophisticated is the model (considering, for example, the rheology of the material), more input data will be required.

We would like to stress the simplicity of the slide model used here as a great advantage regarding parameter set-up. Although the end-user has to adjust some input parameters of the model, within a range of acceptable value, the simplicity of the proposed numerical model makes this task remain simple, not representing an obstacle to run the model. On the other hand, the efficient GPU implementation of the model, allows performing uncertainty quantification (see Snchez-Linares et al. (2016)) on a few parameters, and investigating the sensitivity to them varying on small ranges (as in González-Vida et al. (2019)). This will be the aim of future works. When field or experimental observations are available, a different approach is proposed in Ferreiro-Ferreiro et al. (2020) where an automatic data assimilation strategy for a similar landslide non-hydrostatic model is proposed. The same strategy can be adapted for the model used here.

5.1. Benchmark Problem 4: Two-dimensional submarine granular slide

The first proposed benchmark problem for granular slides, BP4 in the list, aims to reproduce the generation of tsunamis by submarine granular slides modeled in the laboratory experiment by means of glass beads. The corresponding 2D laboratory were performed at the Ecole Centrale de Marseille (see Grilli et al. (2017) for a description of the experiment). A set of 58 (29 with their corresponding replicate) experiments were performed at the IRPHE (Institut de Recherche sur les Phénomenes Hors Equilibre) precision tank. The experiments were performed using a triangular submarine cavity filled with glass beads that were released by lifting a sluice gate and then moving down a plane slope, everything underwater. Figure 2 shows a schematic picture of the experiment set-up. The one-dimensional domain $[0, 6]$ is discretized with $\Delta x = 0.005 \ m$ and wall boundary conditions were imposed. The simulated time is 10 s. The CFL number was set to 0.5 and model parameters take the following values:

$$g = 9.81, \quad r = 0.78, \quad n_a = 0.2, \quad n_m = 10^{-3},$$

$$d_s = 7 \cdot 10^{-3}, \quad \delta_1 = 6°, \quad \delta_2 = 17°, \quad \delta_3 = 12°, \quad \beta = 0.136, \quad \gamma = 10^{-3}.$$
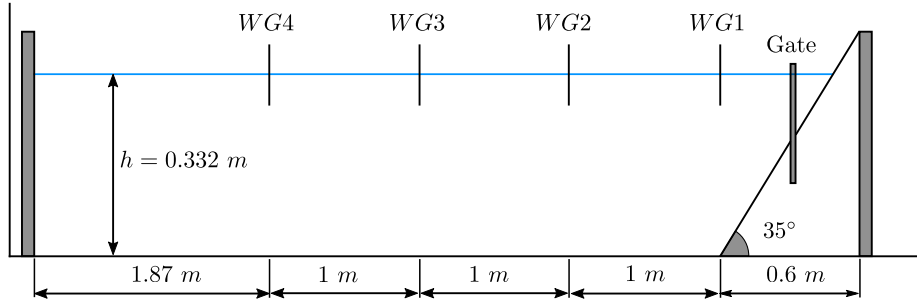
Figure 2: BP4 sketch showing the longitudinal cross section of the IRPHE's precision tank. The figure shows the location of the plane slope, the sluice gate and the 4 gages (WG1, WG2, WG3 WG4).

Figure 3 depicts the modeled times series for the water height at the 4 wave gages and compared them with the lab measured data. Note that the computed free surface matches well with the laboratory data for gauges WG2, WG3,WG4, both in amplitude and frequency. For gauge WG1, some mismatch is observed in amplitude, that could be explained for the simplicity of the landslide model and the absence of turbulent effects in the model.

Figure 4 shows the location and evolution of the granular material and water free surface at several times during the numerical simulation. In Grilli et al. (2017) some snapshots of the landslide evolution are shown at different time steps. In particular it could be seen that the location of the landslide front is well-captured, but there is some mismatch of the landslide shape at the front, mainly due to the simplicity of the landslide model considered here. In particular, we consider that density remains constant in the landslide layer during the simulation, what is not true due to the water entrainment.

In the numerical experiments presented in this section, the number of layers was set up to 5. Similar results were obtained with lower number of layers (4 or 3), but slightly closer to measured data when considering 5 layers. This justifies our choice in the present test problem. Larger number of layers do not further improve the numerical results. This may indicate that to get better numerical results it is not longer a question related with the dispersive properties of the

 model (that improve with the number of layers) but is more likely due to some missing physics.
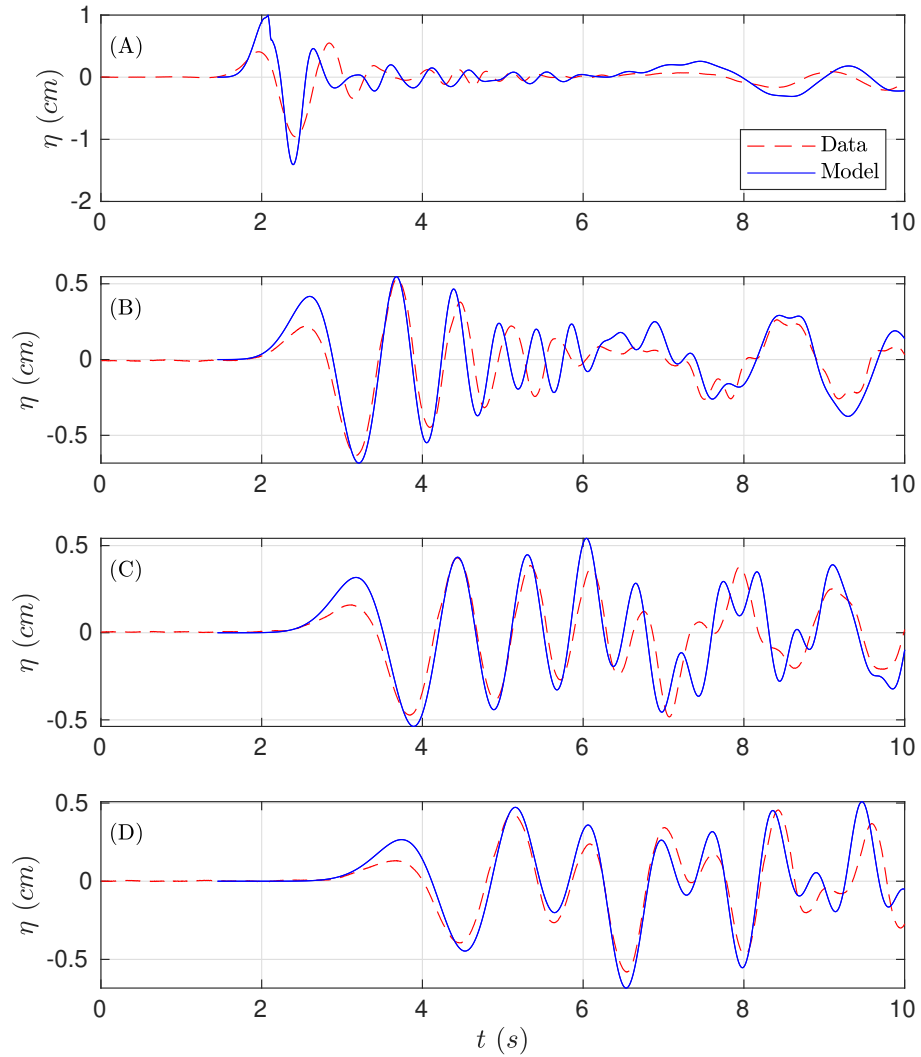
Figure 3: Numerical time series for the simulated water surface (in blue) compared with lab measure data (red) at wave gauges (A) WG1, (B) WG2, (C) WG3, and (D) WG4.
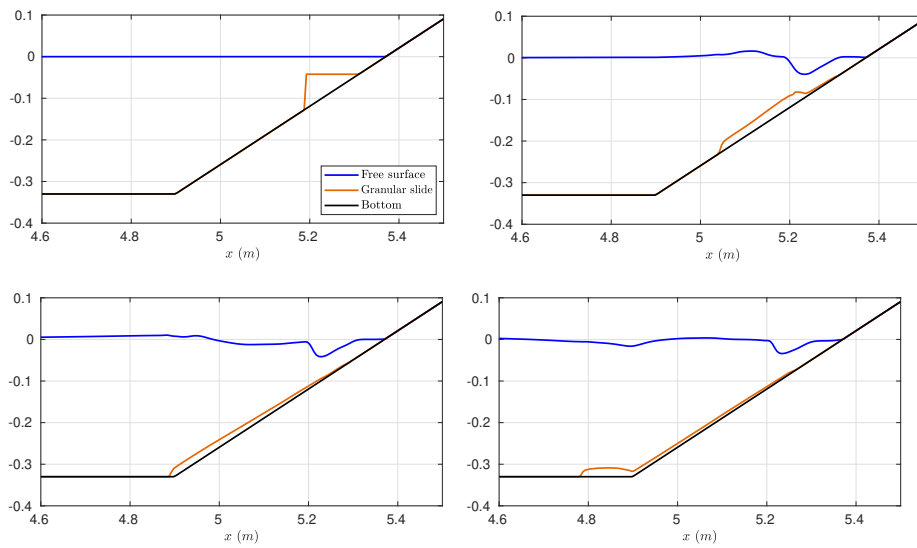
Figure 4: Modeled location of the granular material and water free surface elevation at times $t = 0,\ 0.3,\ 0.6,\ 0.9\ s$.

5.2. Benchmark Problem 5: Two-dimensional subaerial granular slide

389   This benchmark is based on a series of 2D laboratory experiments performed

390   by Viroulet et al. (2014) in a small tank at the École Centrale de Marseille,

391   France. The simplified picture of the set-up for these experiments can be found

in Figure 5. The granular material was confined in triangular subaerial cavities
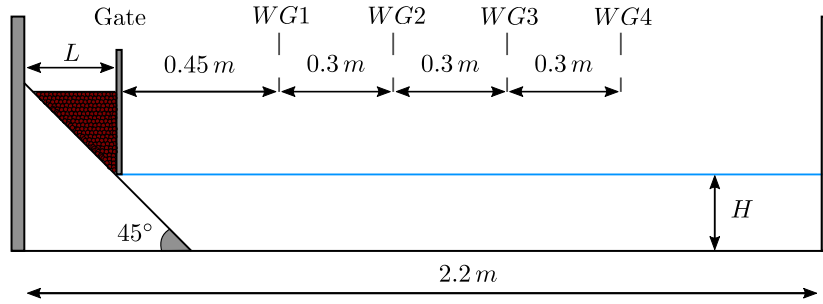
Figure 5: BP5 sketch of the set-up for the laboratory experiments.

392

393   and composed of dry glass beads of diameter d_s (that was varied) and density

394   $\rho_s = 2,500\,km/m^3$. This was located on a plane $45°$ slope just on top of the

395   water surface. Then the slide was released by lifting a sluice gate and entering

396   right away in contact with water. The experimental set-up used by Viroulet

397   et al. (2014) consisted of a wave tank, $2.2\,m$ long, $0.4\,m$ high, and $0.2\,m$ wide.

398   The granular material is initially retained by a vertical gate on the dry slope.

399   The gate is suddenly lowered, and in the numerical experiments, it should be

400   assumed that the gate release velocity is large enough to neglect the time it takes

401   the gate to withdraw. The front face of the granular slide touches the water

402   surface at $t = 0$. The initial slide shape has a triangular cross-section over the

403   width of the tank, with down-tank length L, and front face height $B = L$ as the

404   slope angle is $45°$.

405   For the present benchmark, two cases are considered. Case 1 defined by

406   the following set-up: $d_s = 1.5\ mm$, $H = 14.8\ cm$ and $L = 11\ cm$ and Case 2

407   given by $d_s = 10\ mm$, $H = 15\ cm$ and $L = 13.5\ cm$. The benchmark problem

408   proposed consists of simulating the free surface elevation evolution at the four

409   gauges WG1 to WG4 where measured data are provided, for the two test cases

described above.

The same model configuration as in the previous benchmark problem is used here. The vertical structure is reproduced using three layers in the present case. The one-dimensional domain is given by the interval $[0, 2.2]$ and it is discretized using a step $\Delta x = 0.003\ m$. As boundary conditions, rigid walls were imposed. The simulation time is $2.5\ s$. The CFL number is set to 0.9 and model parameters take the following values:

$$g = 9.81, \quad r = 0.6, \quad n_a = 10^{-2}, \quad n_m = 9 \cdot 10^{-2},$$

$$\delta_1 = 6°, \quad \delta_2 = 26°, \quad \delta_3 = 12°, \quad \beta = 0.136, \quad \gamma = 10^{-3}.$$

Finally d_s was set to $1.5 \cdot 10^{-3}$ and $10 \cdot 10^{-3}$ depending on the test case. Figure 6 shows the comparison for Case 1. In this case, the numerical results show an very good agreement when compared with lab measured data and, in particular, the two leading waves are very well captured. Figure 7 shows the comparison for Case 2. In this case, the agreement is good, but larger differences between model and lab measurements can be observed. Two things can be concluded from the observation of Figures 6 and 7: (1) a much better agreement is obtained for Case 1 than for Case 2 and (2) the agreement is better for gauges located further from the slide compared with closer to the slide gauges. Although paradoxical, this second differential behavior among gauges can be explained as a consequence of the hydrodynamic component being much better resolved and simulated than the morphodynamic component (the movement of the slide material), obviously much more difficult to reproduce. But, at the same time, this implies a correct transfer of energy at the initial stages of the interaction slide/fluid.

Finally, Figure 8 shows the location of the granular material and the free surface elevation at several times for numerical simulation of Case 1. In Viroulet et al. (2014) some snapshots of the landslide evolution are shown at different time-steps that can be compared with Figure 8. As for the benchmark problem 4, it can be seen that the location of the landslide front is well-captured, but there is some mismatch of the landslide shape at the front, mainly due to the simplicity of the landslide model considered here.
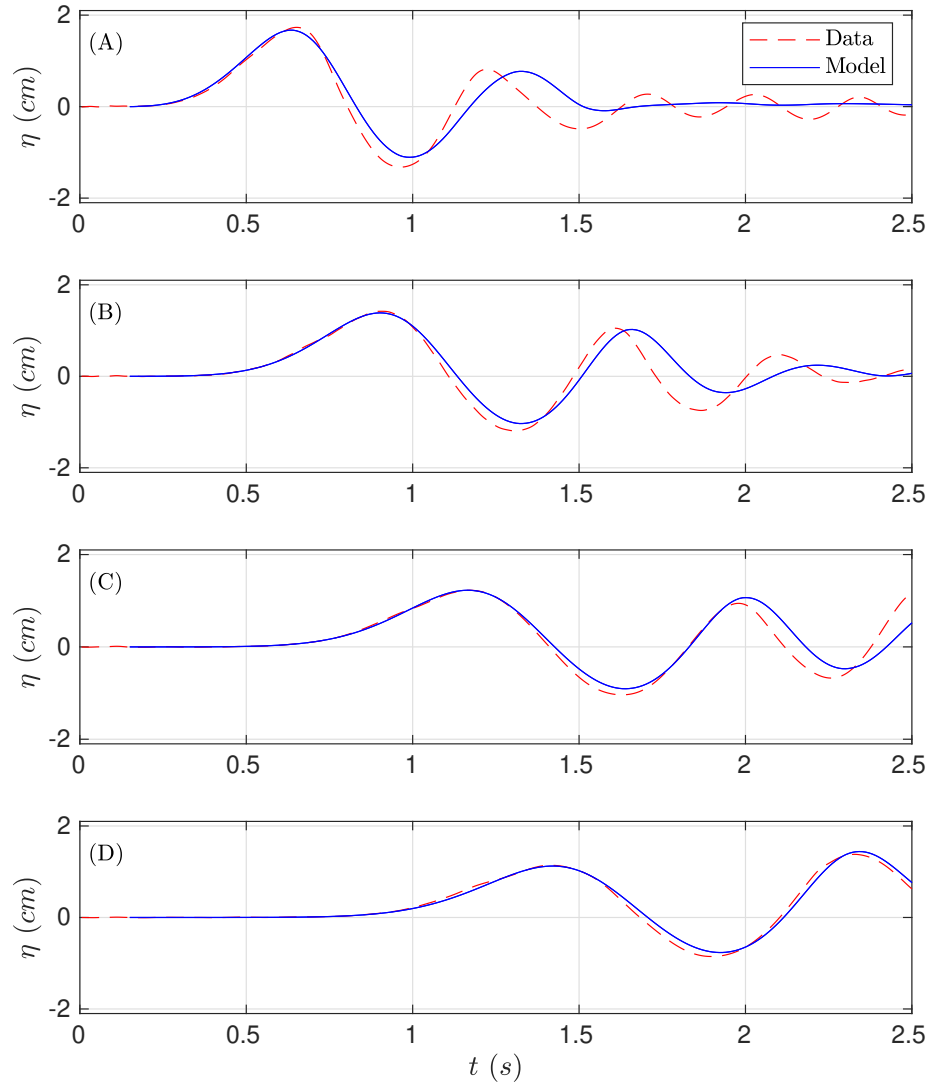
Figure 6: Numerical time series for the simulated water surface (in blue) compared with lab measure data (red). Case 1 at gauges (A) G1, (B) G2, (C) G3, and (D) G4
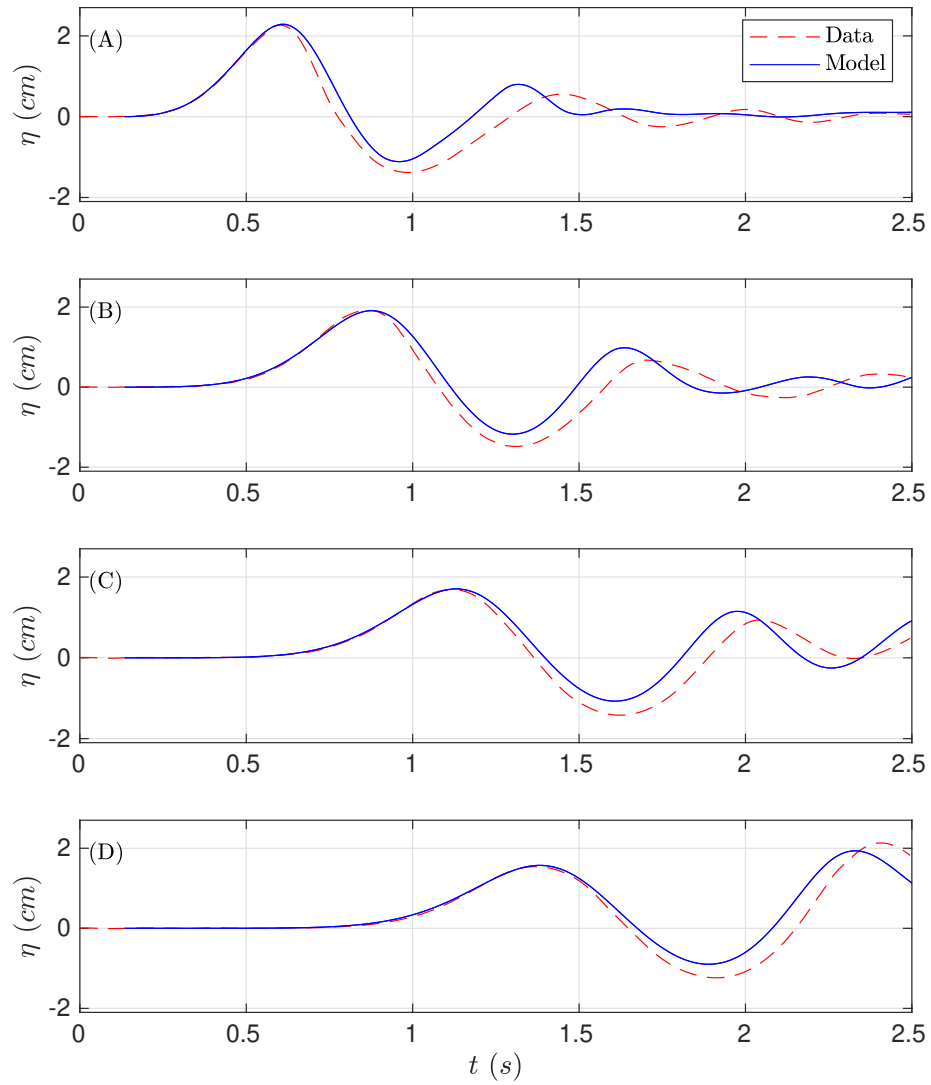
Figure 7: Numerical time series for the simulated water surface (in blue) compared with lab measure data (red). Case 2 at gauges (A) G1, (B) G2, (C) G3, and (D) G4
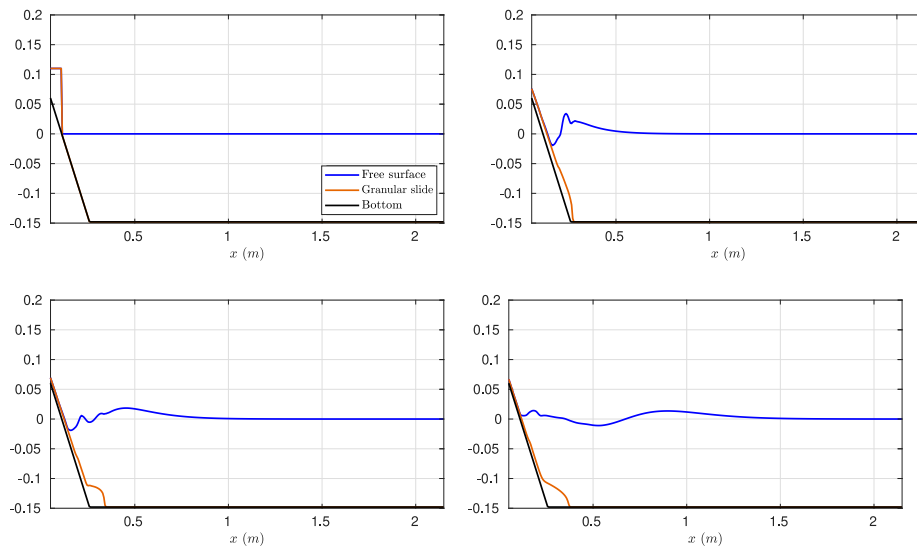
Figure 8: Modelled water free surface elevation and granular slide location at times $t = 0,\ 0.2,\ 0.4,\ 0.8\ s$ for the Case 1.

 5.3. Benchmark Problem 6: Three-dimensional subaerial granular slide

This benchmark problem is based on the 3D laboratory experiment of Mohammed and Fritz (2012) and Mohammed (2010). Benchmark 6 simulates the rapid entry of a granular slide into a 3D water body. The landslide tsunami experiments were conducted at Oregon State University in Corvallis. The landslides are deployed off a plane 27.1° slope, as shown in Figure 9. The landslide
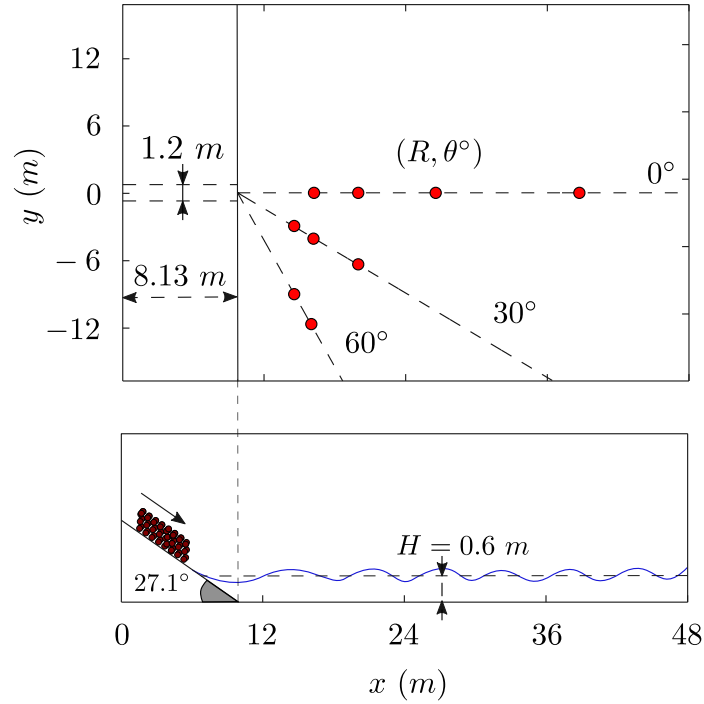
Figure 9: Schematic picture of the computational domain. Plan view in the upper pannel. Cross-section at $y = 0$ m in the lower pannel. The red dots represent the distribution of the wave gauge positions in the laboratory set-up.

material is deployed using a box measuring 2.1 m × 1.2 m × 0.3 m, with a volume of 0.756 m^3 and weighting approximately 1360 kg. The case selected by the NTHMP as benchmarking test is the one with a still water depth of $H = 0.6$ m (see Figure 9). The computational domain is the rectangle defined by $[0, 48] \times [-14, 14]$, and it is discretized with $\Delta x = \Delta y = 0.06$ m. At the boundaries, wall boundary conditions were imposed. The simulation time is 20 s and we set the $CFL = 0.5$. According to Mohammed and Fritz (2012) and

Mohammed (2010), the three-dimensional granular landslide parameters were set to

$$g = 9.81, \quad r = 0.55, \quad n_a = 4, \quad , n_m = 4 \cdot 10^{-2},$$

$$d_s = 13.7 \cdot 10^{-3}, \quad \delta_1 = 6°, \quad \delta_2 = 30°, \quad \delta_3 = 12°, \quad \beta = 0.136, \quad \gamma = 10^{-3}.$$

The vertical structure of the fluid layer is modeled using three layers. Similar results were obtained with 2 layers.

Initially, the slide box is driven using four pneumatic pistons. Here we provide comparisons for the case where the pressure for the pneumatic pistons generating the slide is $P = 0.4$ MPa ($P = 58 \, \text{PSI}$). In Mohammed (2010), it is shown that for this test case, the landslide box reached a velocity of $v_b = 2.3 \cdot \sqrt{g \cdot 0.6} = 5.58 \; m/s$. Thus, the initial condition for the water velocities is set to zero:

$$u_i = 0, \; i = 1, 2, \ldots, L$$

and for the landslide velocity is set to the above-mentioned constant value:

$$u_s = 5.58, \text{wherever } z_s > 0,$$

for the x-component. The y-component of the landslide velocity was initially set to zero.

The benchmark problem proposed consists of simulating the free surface elevation at some wave-gauges. In the present study, we include the comparison for the 9 wave gauges displayed in Figure 9 as red dots. A total number of 21 wave gauges composed the whole set of data, plus 5 run-up gauges. The wave-gauge in coordinates $(R, \theta°)$ are given more precisely in Table 1. Before comparing

$\theta°$	0°				30°			60°	
R	5.12	8.5	14	24.1	3.9	5.12	8.5	3.9	5.12

Table 1: Location of the 9 waves gauges referenced to the toe's slope.

time series, we first check the simulated landslide velocity at impact with the measured one. The slide impact velocity measured in the lab experiment is

⁴⁷³ 5.72 m/s at time $t = 0.44$ s. The numerically computed slide impact velocity

⁴⁷⁴ is slightly underestimated with a value of 5.365 m/s at time $t = 0.4$ s as it can

⁴⁷⁵ be seen in the upper panel of Figure 10. The final simulated granular deposit is

⁴⁷⁶ located partially on the final part of the sloping floor and partially at the flat

⁴⁷⁷ bottom closer to the point of change of slope as it is shown in the lower panel of

⁴⁷⁸ Figure 10. This can be compared with the actual final location of the granular

⁴⁷⁹ material in the experimental setup. The simulated deposits extend further, be-

⁴⁸⁰ ing thinner. This is probably due to the fact that we are neglecting the friction

⁴⁸¹ that it is produced by the change in the slope at the transition area. In Ma

et al. (2015) a similar result and discussion can be found. Figure 11 presents
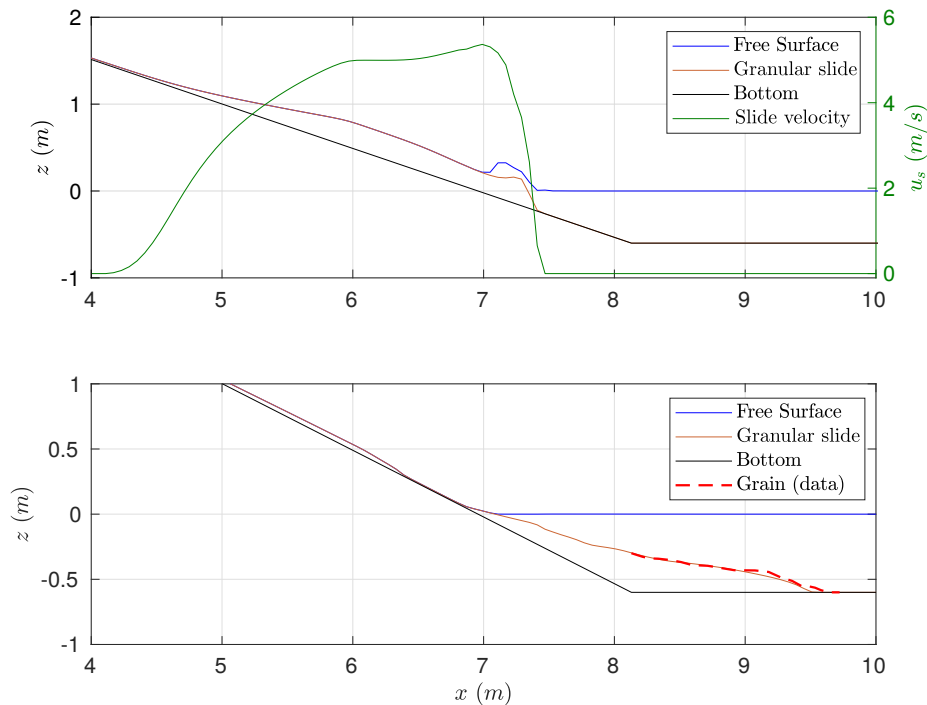
Figure 10: BP6. Cross-section at $y = 0$ m. Upper panel shows the location and velocity of the granular slide and the generated wave at time $t = 0.4$ s from the triggering and lower panel the final deposit location (at $t = 20$ s).

⁴⁸²

⁴⁸³ the comparisons between simulated and the measured waves at the 9 gauges

⁴⁸⁴ we have retained. Model results are in good agreement with measured time.

⁴⁸⁵ Despite this, wave heights are overestimated at some stations, specially those

closer to the shoreline (for example, the station with $R = 3.9$ and $\theta = 30°$). This effect has been also observed and discussed in Ma et al. (2015). At some of the time series, it can be observed that the small free-surface oscillations at the final part of the time series, are not well-captured by the model. This is partially due to the relatively coarse horizontal grids used in the simulation. These same behaviour can be also observed in Figure 12 in this case for the comparisons between simulated and measured run-up values at some measure locations situated at the shoreline (as for $x = 7.53$).

Table 2 shows the wall-clock times on a NVIDIA Tesla P100 GPU. It can be observed that including non-hydrostatic terms in the SWE-SH system results in an increase of the computational time in 2.9 times. If a richer vertical structure is considered, then larger computational times are required. As examples for the two and three-layer systems, 3.48 and 4.66 times increase in the computational effort.

	Runtime (s)	Ratio
SWE-SH	186.55	1
1L NH-SH	541.11	2.9
2L NH-SH	649.19	3.48
3L NH-SH	869.32	4.66

Table 2: Wall-clock times in seconds for the SWE-SH and the non-hydrostatic GPU implementations. The ratios are with respect the SWE-SH model implementation.
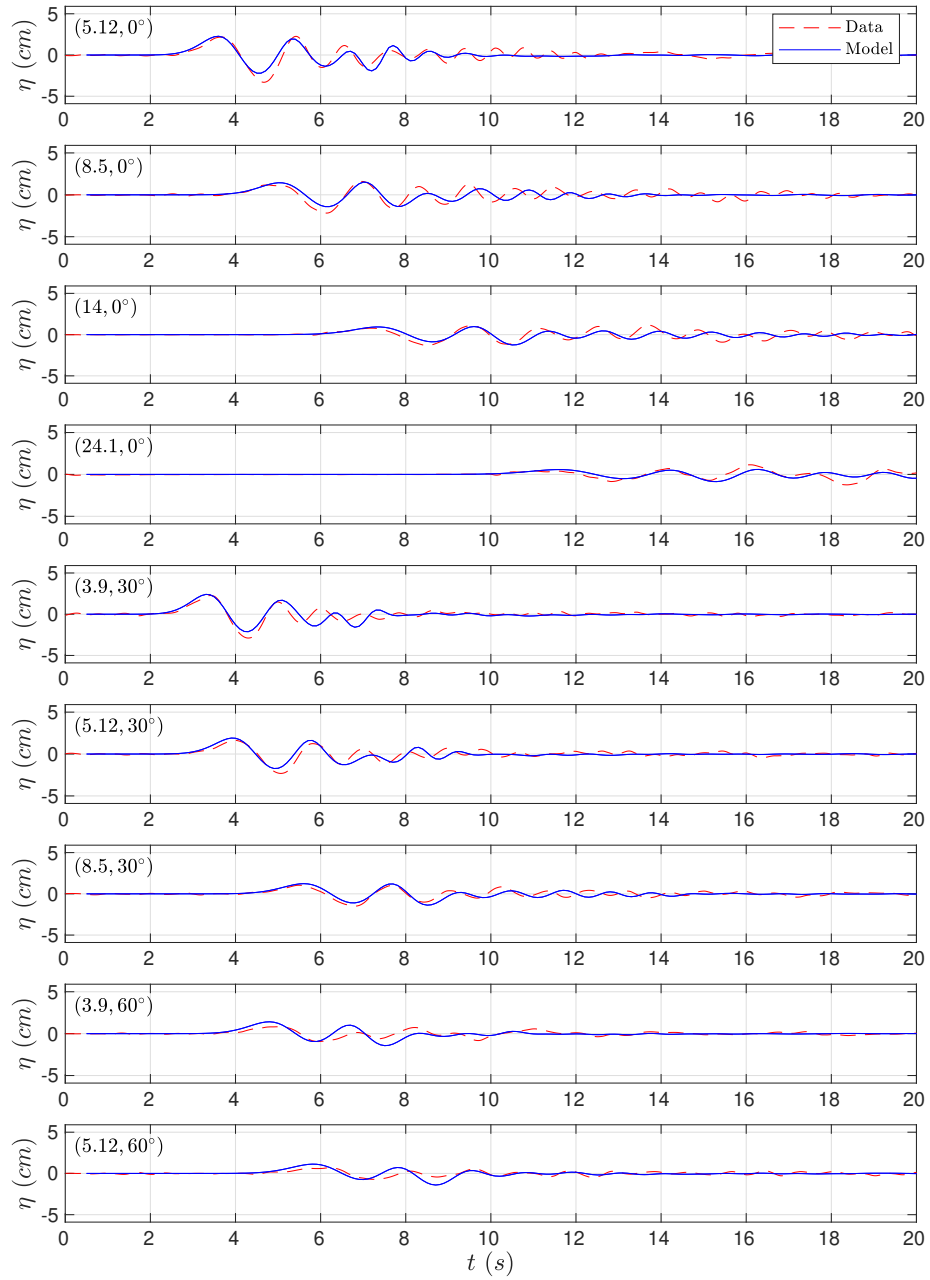
Figure 11: Simulated (solid blue lines) time series compared with measured (dashed red lines) free surface waves for the 9 wave gauges considered at (R, θ°) positions.
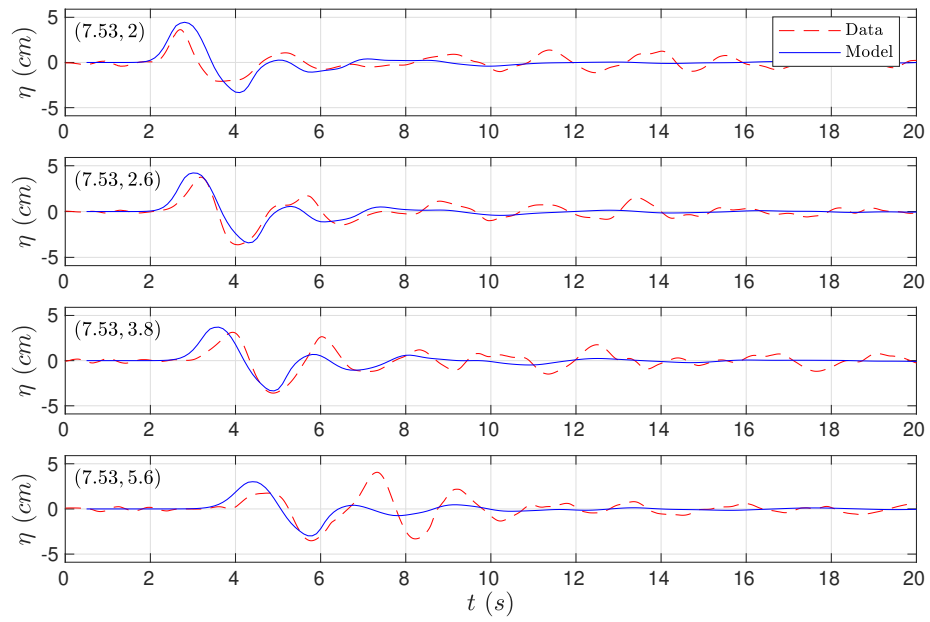
Figure 12: Time series comparing numerical run-up (solid blue) at the 4 run-up gauges with the measured (dashed red) data at (x, y) positions.

6. Concluding Remarks

Numerical models need to be validated previous to their use as predictive tools. This requirement becomes even more necessary when these models are going to be used for risk assessment in natural hazards where human lives are involved. The current work aims at benchmarking the novel Multilayer-HySEA model for landslide generated tsunamis produced by granular slides, in order to provide in the future to the tsunami community with a robust, efficient and reliable tool for landslide tsunami hazard assessment.

The Multilayer-HySEA code implements a two-phase model to describe the interaction between landslides (aerial or subaerial) and water body. The upper phase describes the hydrodynamic component. This is done using a stratified vertical structure that includes non-hydrostatic terms in order to include dispersive effects in the propagation of simulated waves. The motion of the landslide is taken into account by the lower phase, consisting of a Savage-Hutter model. To reproduce these flows, the friction model given in Pouliquen and Forterre (2002) is considered here. The hydrodynamic and morphodynamic models are weakly-coupled through the boundary condition at their interface.

The implemented numerical algorithm combines a finite volume path-conservative scheme for the underlying hyperbolic system and finite differences for the discretization of the non-hydrostatic terms. The numerical model is implemented to be run in GPU architectures. The two-layer non-hydrostatic code coupled with the Savage-Hutter used here, has been shown to run at very efficient computational times. To assess this, we compare with respect to the one-layer SWE/Savage-Hutter GPU code. For the numerical simulations performed here, the execution times for the non-hydrostatic model are always below 4.66 times the times for the SWE model for a number of layers up to three. We can conclude that the numerical scheme presented here is very robust, extremely efficient, and can model dispersive effects generated by submarine/subaerial landslides at a low computational cost considering that dispersive effects and a vertical multilayer structure are included in the model. Model results show

a good agreement with the experimental data for the three benchmark problems considered. In particular, for BP5, but this also occurs for the other two benchmark problems. In general, it is shown a better agreement for the hydrodynamic component, compare with their morphodynamic counterpart, which is more challenging to reproduce.

7. Code and data availability

The numerical code is currently under development and only available to close collaborators. In the future, we will provide an open version of the code as we already do for Tsunami-HySEA. This version will be downloaded from https://edanya.uma.es/hysea/index.php/download.

All the data used in the current work, necessary to reproduce the set-up of the numerical experiments and the laboratory measured data reauired to compared with, can be downloaded from LTMBW (2017) at http://www1.udel.edu/kirby/landslide/. Finally, the NetCDF files containing the numerical results obtained with the Multilayer-HySEA code for all the tests presented here can be found and download from Macías et al. (2020b).

8. Authors' contributions

JM is leading the HySEA codes benchmarking effort undertaken by the EDANYA group, he wrote most of the paper, reviewed and edited it, assisted in the numerical experiments and in their set up. CE implemented the numerical code and performed all the numerical experiments, he also contributed to the writing of the manuscript. JM and CE did all the figures. MC strongly contributed to the design and implementation of the numerical code.

9. Competing interest

The authors declare that they have no conflict of interest.

10. Acknowledgements

This research has been partially supported by the Spanish Government-FEDER funded project MEGAFLOW (RTI2018-096064-B-C21), the Junta de Andalucía-FEDER funded project UMA18-Federja-161 and the University of Málaga, Campus de Excelencia Internacional Andalucía Tech.

References

Abadie, S., Morichon, D., Grilli, S., Glockner, S., 2010. Numerical simulation of waves generated by landslides using a multiple-fluid Navier–Stokes model. Coastal Engineering 57 (9), 779 – 794.

Abadie, S. M., Harris, J. C., Grilli, S. T., Fabre, R., 2012. Numerical modeling of tsunami waves generated by the flank collapse of the Cumbre Vieja Volcano (La Palma, Canary Islands): Tsunami source and near field effects. Journal of Geophysical Research: Oceans 117 (C5).

Adsuara, J., Cordero-Carrión, I., Cerdá-Durán, P., Aloy, M., 2016. Scheduled relaxation Jacobi method: Improvements and applications. Journal of Computational Physics 321, 369–413.

Ataie-Ashtiani, B., Najafi-Jilani, A., 2008. Laboratory investigations on impulsive waves caused by underwater landslide. Coastal Engineering 55 (12), 989 – 1004.

Ataie-Ashtiani, B., Shobeyri, G., 2008. Numerical simulation of landslide impulsive waves by incompressible smoothed particle hydrodynamics. International Journal for Numerical Methods in Fluids 56 (2), 209–232.

Brunet, M., Moretti, L., Le Friant, A., Mangeney, A., Fernández Nieto, E. D., Bouchut, F., Jun 2017. Numerical simulation of the 30–45ka debris avalanche flow of Montagne Pelée volcano, Martinique: from volcano flank collapse to submarine emplacement. Natural Hazards 87 (2), 1189–1222.

581 Castro, M., Fernández-Nieto, E., 2012. A Class of Computationally Fast First
582   Order Finite Volume Solvers: PVM Methods. SIAM Journal on Scientific
583   Computing 34 (4), A2173–A2196.

584 Castro, M., Ortega, S., de la Asunción, M., Mantas, J., Gallardo, J., 2011. GPU
585   computing for shallow water flow simulation based on finite volume schemes.
586   Comptes Rendus Mécanique 339 (2–3), 165–184.

587 Escalante, C., Fernández-Nieto, E., Morales, T., Castro, M., 2018a. An efficient
588   two–layer non–hydrostatic approach for dispersive water waves. Journal of
589   Scientific Computing.

590 Escalante, C., Morales, T., Castro, M., 2018b. Non-hydrostatic pressure shallow
591   flows: GPU implementation using finite volume and finite difference scheme.
592   Applied Mathematics and Computation 338, 631 – 659.

593 Fernández-Nieto, E., Bouchut, F., Bresch, D., Castro, M., Mangeney, A., 2008.
594   A new Savage-Hutter type model for submarine avalanches and generated
595   tsunami. Journal of Computational Physics 227 (16), 7720–7754.

596 Fernández-Nieto, E., Parisot, M., Penel, Y., Sainte-Marie, J., 2018. A hierarchy
597   of dispersive layer-averaged approximations of Euler equations for free surface
598   flows. Communications in Mathematical Sciences 16 (5), 1169–1202.

599 Ferreiro-Ferreiro, A., Garca-Rodrguez, J., Lpez-Salas, J., Escalante, C., Castro,
600   M., 2020. Global optimization for data assimilation in landslide tsunami
601   models. Journal of Computational Physics 403, 109069.
602   URL   `http://www.sciencedirect.com/science/article/pii/`
603   `S0021999119307740`

604 Fine, I. V., Rabinovich, A. B., Kulikov, E. A., July 1998. Numerical modelling of
605   landslide generated tsunamis with application to the Skagway Harbor tsunami
606   of November 3, 1994. In: Proc. Intl. Conf. on Tsunamis. Paris, pp. 211–223.

Fritz, H. M., Hager, W. H., Minor, H.-E., 2004. Near field characteristics of landslide generated impulse waves. Journal of Waterway, Port, Coastal, and Ocean Engineering 130 (6), 287–302.

Garres-Daz, J., Fernndez-Nieto, E. D., Mangeney, A., de Luna, T. M., 2020. A weakly non-hydrostatic shallow model for dry granular flows.

González-Vida, J., Macías, J., Castro, M., Sánchez-Linares, C., Ortega, S., Arcas, D., 2019. The Lituya Bay landslide-generated mega-tsunami. Numerical simulation and sensitivity analysis. Nat. Hazards Earth Syst. Sci. 19, 369–388.

Grilli, S. T., Shelby, M., Kimmoun, O., Dupont, G., Nicolsky, D., Ma, G., Kirby, J. T., Shi, F., Mar 2017. Modeling coastal tsunami hazard from submarine mass failures: effect of slide rheology, experimental validation, and case studies off the US East Coast. Natural Hazards 86 (1), 353–391.

Harbitz, C. B., Pedersen, G., Gjevik, B., 1993. Numerical simulations of large water waves due to landslides. Journal of Hydraulic Engineering 119 (12), 1325–1342.

Heinrich, P., 1992. Nonlinear water waves generated by submarine and aerial landslides. Journal of Waterway, Port, Coastal, and Ocean Engineering 118 (3), 249–266.

Heller, V., Hager, W., 2010. Impulse product parameter in landslide generated impulse waves. Journal of Waterway, Port, Coastal, and Ocean Engineering 136 (3), 145–155.

Horrillo, J., Wood, A., Kim, G.-B., Parambath, A., 2013. A simplified 3-D Navier-Stokes numerical model for landslide-tsunami: Application to the Gulf of Mexico. Journal of Geophysical Research: Oceans 118 (12), 6934–6950.

Kirby, J. T., Grilli, S. T., Zhang, C., Horrillo, J., Nicolsky, D., Liu, P. L.-F., 2018. The NTHMP landslide tsunami benchmark workshop, Galveston, January 9-11, 2017. Tech. rep., Research Report CACR-18-01.

Kirby, J. T., Shi, F., Nicolsky, D., Misra, S., Dec 2016. The 27 April 1975 Kitimat, British Columbia, submarine landslide tsunami: a comparison of modeling approaches. Landslides 13 (6), 1421–1434.

LTMBW, 2017. Landslide Tsunami Model Benchmarking Workshop, Galveston, Texas, 2017. `http://www1.udel.edu/kirby/landslide/index.html`, accessed: 2020-04-11.

Ma, G., Kirby, J. T., Hsu, T.-J., Shi, F., 2015. A two-layer granular landslide model for tsunami wave generation: Theory and computation. Ocean Modelling 93 (C), 40–55.

Ma, G., Kirby, J. T., Shi, F., 2013. Numerical simulation of tsunami waves generated by deformable submarine landslides. Ocean Modelling 69 (Complete), 146–165.

Ma, G., Shi, F., Kirby, J. T., 2012. Shock-capturing non-hydrostatic model for fully dispersive surface wave processes. Ocean Modelling 43-44, 22 – 35.

Macías, J., Castro, M., Ortega, S., Escalante, C., González-Vida, J., Jun 2017. Performance benchmarking of Tsunami-HySEA model for NTHMP's inundation mapping activities. Pure and Applied Geophysics.

Macías, J., Escalante, C., Castro, M., 2020a. Multilayer-HySEA model validation for landslide generated tsunamis. Part I Rigid slides. Nat. Hazards Earth Syst. Sci. Discuss.

Macías, J., Escalante, C., Castro, M., 2020b. Numerical results in Multilayer-HySEA model validation for landslide generated tsunamis. Part II Granular slides. Dataset on Mendeley, doi: 10.17632/94txtn9rvw.2.

Macías, J., Escalante, C., Castro, M., 2020c. Performance assessment of Tsunami-HySEA model for NTHMP tsunami currents benchmarking. laboratory data. Coastal Engineering 158 (103667).

Macías, J., Escalante, C., Castro, M., González-Vida, J., Ortega, S., 2017. HySEA model. Landslide Benchmarking Results. NTHMP report. Tech. rep., Universidad de Málaga.

Macías, J., Ortega, S., González-Vida, J., Castro, M., 2020d. Performance assessment of Tsunami-HySEA model for NTHMP tsunami currents benchmarking. field cases. Ocean Modeling 152, 101645.

Macías, J., Vázquez, J., Fernández-Salas, L., González-Vida, J., Bárcenas, P., Castro, M., del Río, V. D., Alonso, B., 2015. The Al-Borani submarine landslide and associated tsunami. A modelling approach. Marine Geology 361, 79 – 95.

Mangeney, A., Bouchut, F., Thomas, N., Vilotte, J. P., Bristeau, M. O., 2007. Numerical modeling of self-channeling granular flows and of their levee-channel deposits. Journal of Geophysical Research: Earth Surface 112 (F2).

Mohammed, F., 2010. Physical modeling of tsunamis generated by three-dimensional deformable granular landslides. Ph.D. thesis, Georgia Institute of Technology.

Mohammed, F., Fritz, H. M., 2012. Physical modeling of tsunamis generated by three-dimensional deformable granular landslides. Journal of Geophysical Research: Oceans 117 (C11).

Pouliquen, O., Forterre, Y., 2002. Friction law for dense granular flows: application to the motion of a mass down a rough inclined plane. Journal of Fluid Mechanics 453, 133151.

Rzadkiewicz, S. A., Mariotti, C., Heinrich, P., 1997. Numerical simulation of submarine landslides and their hydraulic effects. Journal of Waterway, Port, Coastal, and Ocean Engineering 123 (4), 149–157.

Savage, S., Hutter, K., 1 1989. The motion of a finite mass of granular material down a rough incline. J. Fluid Mech. 199, 177–215.

Snchez-Linares, C., de la Asuncin, M., Castro, M., Vida, J. G., Macas, J., Mishra, S., 12 2016. Uncertainty quantification in tsunami modeling using multi-level monte carlo finite volume method. Journal of Mathematics in Industry 6.

Viroulet, S., Sauret, A., Kimmoun, O., 2014. Tsunami generated by a granular collapse down a rough inclined plane. EPL (Europhysics Letters) 105 (3), 34004.
URL http://stacks.iop.org/0295-5075/105/i=3/a=34004

Weiss, R., Fritz, H. M., Wünnemann, K., 2009. Hybrid modeling of the mega-tsunami runup in Lituya Bay after half a century. Geophysical Research Letters 36 (9).

Yavari-Ramshe, S., Ataie-Ashtiani, B., Dec 2016. Numerical modeling of sub-aerial and submarine landslide-generated tsunami waves–recent advances and future challenges. Landslides 13 (6), 1325–1368.